

Numerical Study To Assess Sulfur Hexafluoride as a Medium for Testing Multielement Airfoils

*Daryl L. Bonhaus and W. Kyle Anderson
Langley Research Center • Hampton, Virginia*

*Dimitri J. Mavriplis
Institute for Computer Applications in Science and Engineering
Langley Research Center • Hampton, Virginia*

Available electronically at the following URL address: <http://techreports.larc.nasa.gov/ltrs/ltrs.html>

Printed copies available from the following:

NASA Center for AeroSpace Information
800 Elkridge Landing Road
Linthicum Heights, MD 21090-2934
(301) 621-0390

National Technical Information Service (NTIS)
5285 Port Royal Road
Springfield, VA 22161-2171
(703) 487-4650

Abstract

A methodology is described for computing viscous flows of air and sulfur hexafluoride (SF₆). The basis of the method is an existing flow solver that calculates turbulent flows in two dimensions on unstructured triangular meshes. The solver has been modified to incorporate the thermodynamic model for SF₆ and used to calculate the viscous flow over two multielement airfoils that have been tested in a wind tunnel with air as the test medium. Flows of both air and SF₆ at a free-stream Mach number of 0.2 and a Reynolds number of 9×10^6 are computed for a range of angles of attack corresponding to the wind-tunnel test. The computations are used to investigate the suitability of SF₆ as a test medium in wind tunnels and are a follow-on to previous computations for single-element airfoils. Surface-pressure, lift, and drag coefficients are compared with experimental data. The effects of a heavy gas on the details of the flow are investigated based on computed boundary-layer and skin-friction data. In general, the predictions in SF₆ vary little from those in air. Within the limitations of the computational method, the results are sufficiently encouraging to warrant further experiments.

Introduction

Although the capability to test three-dimensional configurations at full-scale flight Reynolds numbers is limited, it is particularly critical in high-lift systems because an accurate design depends upon the ability to vary the Mach and Reynolds numbers independently. Test results at a low Reynolds number cannot be extrapolated for high-lift systems where viscous effects are important. (See refs. 1 and 2.) Cryogenic temperatures, pressurized tunnels, and combinations of these techniques have been used to increase the Reynolds number capability of wind tunnels. Cryogenic testing is a developing technology; however, the capability does not yet exist to test cheaply and frequently enough for preliminary aircraft design purposes. Pressurized tunnels, with air as the test medium, fall well short of flight Reynolds numbers, especially as transport aircraft size has increased. An alternative to these methods to achieve higher Reynolds numbers is to test in a gas other than air.

Heavy gases (so called due to their high molecular weight) are an attractive alternative because higher Reynolds numbers can be achieved over those in air at the same free-stream pressures and temperatures. (See ref. 3.) Sulfur hexafluoride (SF₆) has been investigated because its high molecular weight and low speed of sound allow the achievement of Reynolds numbers more than two times higher than those possible in air. In addition, it is odorless, colorless, nonflammable, nontoxic, and essentially inert. (See ref. 4.)

Air in most applications can be assumed to act as an ideal gas; however, this assumption is not true for SF₆, which is both thermally and calorically imperfect. Results obtained with SF₆ will, in general, differ from results obtained with air at the same flow conditions due

to the differing thermodynamic properties. Effective use of SF₆ as a test gas requires a procedure to modify the flow conditions and/or scale the results to represent flow in air. Preliminary computational work has been done (refs. 5 and 6) to quantify the effects of the differing thermodynamic properties of air and SF₆ for both inviscid and viscous flows over airfoils. Reference 5 also presents a Mach number scaling procedure derived from transonic small-disturbance theory that correlates air and SF₆ surface pressures for inviscid flows.

The intent of the current study is to extend the computational database of flows in SF₆ established in reference 5 by performing viscous calculations on multielement airfoils. This extension is necessary to assess the effects of SF₆ on the complex flow fields of high-lift systems. The Mach number scaling mentioned earlier, which is strictly applicable under small-disturbance assumptions, is used to determine applicability of the scaling to highly viscous flows over multielement sections. Descriptions of the original flow solver and of the modifications necessary to simulate heavy gases are presented first, followed by a more detailed discussion of the Mach number scaling procedure. Next, two test configurations used in the current study are presented. Comparisons of surface-pressure, skin-friction, and force data in air and SF₆ are then presented. Also included are experimental surface pressure and force data from a tunnel test in air.

Symbols

A	scaling factor
a	speed of sound, m/sec
$\bar{a}_p, \bar{b}_i, \bar{c}_p, d$	coefficients for equation of state for SF ₆

C_d	section drag coefficient, $\frac{\text{Drag}}{\frac{1}{2}\rho u_\infty^2 c}$
C_f	skin-friction coefficient, $\frac{\text{Shear stress}}{\frac{1}{2}\rho u_\infty^2}$
C_i	coefficients in curve fit for ideal-gas specific heat C_v
c_l	section lift coefficient, $\frac{\text{Lift}}{\frac{1}{2}\rho u_\infty^2 c}$
c_p	pressure coefficient, specific heat at constant pressure, J/kg-K
c_v	specific heat at constant volume, J/kg-K
c	chord length, m
h	specific enthalpy, J/kg
i	summation index
k	constant in equation of state for SF ₆
M	Mach number, $\frac{u_\infty}{a_\infty}$
N_{Re}	Reynolds number, $\frac{\rho_\infty u_\infty c}{\mu_\infty}$
p	pressure, N/m ²
R	gas constant, J/kg-K
S	entropy, J/K
T	temperature, K
u	velocity, m/sec
v	specific volume, m ³ /kg
X, Y	Cartesian coordinates, m
α	angle of attack, deg
γ	ratio of specific heats, $\frac{c_p}{c_v}$
γ'	effective gamma for transonic scaling
ϵ	internal energy per mass, J/kg
ζ	distance normal to airfoil surface normalize by chord length (fig. 12)
κ	transonic similarity parameter
μ	molecular viscosity, N-sec/m ²
ρ	density, kg/m ³
τ	airfoil thickness ratio

Subscripts:

c	thermodynamic properties at critical point
∞	free-stream conditions

Superscript:

$^\circ$	variable as defined for an ideal gas
----------	--------------------------------------

Code Description

Navier-Stokes Solver

A detailed description of the code chosen for this study is given in reference 7. A brief description of the code is given in this section.

The flow solver efficiently calculates turbulent viscous flows over multiple bodies. The code uses an unstructured-grid methodology to integrate the time-dependent two-dimensional Reynolds-averaged Navier-Stokes equations to a steady-state solution.

To generate grids, a panel code is used to create approximate wake lines behind each element. Then, a structured C-mesh is generated around each element and its corresponding wake line. These grids are overlaid, and excess points in the far field are filtered out based on the aspect ratios of the structured-grid cells. The resulting set of points is then triangulated with a modified Delaunay triangulation that allows for stretched triangles. Portions of these C-meshes are also used for the turbulence model, as described later. Figure 1 shows a portion of the resulting triangular mesh; however, this figure is for demonstration only and does not represent the finest level of grid refinement used for the calculations in this report.

The spatial scheme is a finite-element Galerkin discretization that is equivalent to a conventional second-order central-difference scheme on structured grids. Flow quantities are stored at cell vertices. A scalar artificial dissipation model, which is a blend of a Laplacian and a biharmonic operator, is used to avoid spurious oscillations in regions with sharp gradients and to maintain numerical stability. A no-slip condition is enforced on the airfoil surface, which can either be insulated (i.e., no heat transfer through the surface) or held at a constant temperature. The outer boundary of the computational domain is set to the free stream.

The code employs an explicit, five-stage Runge-Kutta algorithm to advance the solution in pseudo time to a steady state. Local time-stepping, implicit residual smoothing, and multigrid techniques are used to accelerate temporal convergence. This combination of an explicit algorithm and convergence acceleration results in a highly efficient code.

The flow is modeled as fully turbulent with the Baldwin-Lomax algebraic turbulence model. (See ref. 8.) This model provides good results for attached flows but is considered inaccurate for flows with large regions of

separation. The model determines the turbulent viscosity based primarily on vorticity and is not directly influenced by thermodynamic properties; for this reason, model accuracy is believed equivalent whether the gas is air or SF₆. The validity of this assumption can be determined only by experimental means.

Because the turbulence model requires data along a line normal to the surface of the airfoil, the original, structured C-meshes are used. Flow-field data are interpolated from the unstructured mesh to the background structured mesh. The turbulence model is executed on these background meshes, and the resulting eddy viscosities are interpolated onto the original triangular mesh.

Heavy-Gas Modifications

If two thermodynamic state variables of an equilibrium gas are known, then all other state variables can be calculated by using relations of classical thermodynamics. These relations involve various partial derivatives of the equation of state (ref. 4), which for SF₆ is given as

$$p = \frac{RT}{v-d} + \sum_{i=2}^5 \frac{\bar{a}_i + \bar{b}_i T + \bar{c}_i \exp(-kT/T_c)}{(v-d)^i} \quad (1)$$

where

$$\begin{aligned} k &= 6.883022 \\ T_c &= 318.8 \text{ K} \\ d &= 3.27367367 \times 10^{-4} \text{ m}^3/\text{kg} \\ \bar{a}_2 &= -49.9051433 \text{ N-m}^4/\text{kg}^2 \\ \bar{b}_2 &= 5.485495 \times 10^{-2} \text{ N-m}^4/\text{kg}^2\text{-K} \\ \bar{c}_2 &= -2.3759245 \times 10^3 \text{ N-m}^4/\text{kg}^2 \\ \bar{a}_3 &= 4.124606 \times 10^{-2} \text{ N-m}^7/\text{kg}^3 \\ \bar{b}_3 &= -3.340088 \times 10^{-5} \text{ N-m}^7/\text{kg}^3\text{-K} \\ \bar{c}_3 &= 2.819595 \text{ N-m}^7/\text{kg}^3 \\ \bar{a}_4 &= -1.612953 \times 10^{-5} \text{ N-m}^{10}/\text{kg}^4 \\ \bar{b}_4 &= 0 \\ \bar{c}_4 &= 0 \\ \bar{a}_5 &= -4.899779 \times 10^{-11} \text{ N-m}^{13}/\text{kg}^5 \\ \bar{b}_5 &= 1.094195 \times 10^{-11} \text{ N-m}^{13}/\text{kg}^5\text{-K} \\ \bar{c}_5 &= -3.082731 \times 10^{-7} \text{ N-m}^{13}/\text{kg}^5 \end{aligned}$$

The temperature dependence of the ideal-gas specific heat at constant pressure is represented by a curve fit (ref. 4) as follows:

$$C_p^\circ = C_1 + C_2 T + C_3 T^2 + C_4 T^3 + C_5 / T^2 \quad (2)$$

where

$$\begin{aligned} C_1 &= -107.9122479 \text{ J/kg-K} \\ C_2 &= 3.94226447 \text{ J/kg-K}^2 \\ C_3 &= -5.128665 \times 10^{-3} \text{ J/kg-K}^3 \\ C_4 &= 2.422895 \times 10^{-6} \text{ J/kg-K}^4 \\ C_5 &= -9.6020764 \times 10^5 \text{ J-K/kg} \end{aligned}$$

The molecular viscosity depends linearly on the temperature and is given by

$$\mu = 5.49 \times 10^{-8} T - 7.877 \times 10^{-7} \quad (3)$$

where T is given in kelvins and μ is given in kilograms per meter per second. A power law formulation is used for the thermal conductivity

$$k = 6.45291 \times 10^{-5} T^{0.942} \quad (4)$$

where k is given in newtons per second per kelvin. The equations for molecular viscosity and thermal conductivity are obtained from a technical bulletin supplied by General Chemical. With this information and the relations from thermodynamic theory, all thermodynamic state variables can be determined after two state variables are given.

First, the code was modified to accept the free-stream pressure and temperature as user-specified parameters. A subroutine was added to calculate all needed thermodynamic state variables in the free stream based on these values; then, a Newton-Raphson iteration was used to calculate the free-stream density from the equation of state, and the other state variables were calculated with explicit relations.

Because the algorithm integrates time-dependent conservation laws for density and energy, these two variables can be used conveniently to determine the other thermodynamic state variables, such as pressure, temperature, entropy, and enthalpy. At each stage of the Runge-Kutta scheme, the internal energy is found by subtracting the kinetic energy from the total energy calculated by the flow solver. The temperature is determined by using the Newton-Raphson iteration to solve an implicit nonlinear

equation. This equation is an explicit formulation for internal energy (ref. 5) and is given by

$$\epsilon = \int C_v^\circ dT + \sum_{i=2}^5 \frac{\bar{a}_i + (1 + kT/T_c) \bar{c}_i \exp(-kT/T_c)}{(i-1)(v-d)^{i-1}} \quad (5)$$

Here,

$$C_v^\circ = C_p^\circ - R \quad (6)$$

is used in the integral to determine the appropriate contribution of the internal energy as if it acted as an ideal gas; the second term accounts for the deviation from the ideal-gas state and is called a *departure function*. (See ref. 9.) After the temperature is known, the other thermodynamic state variables can be calculated explicitly from the density and temperature.

Inviscid Mach Number Scaling

As mentioned earlier, SF₆ is a nonideal gas. The impact of this fact on inviscid flow in the transonic speed regime is demonstrated in figure 2; the pressure distribution is shown for NACA airfoil 0012 at a free-stream Mach number of 0.8 and an angle of attack of 1.25°, which corresponds to AGARD test case 01. (See ref. 10.) The results were obtained by running the code in an inviscid mode. The results for air show a strong shock on the upper surface and a weak shock on the lower surface. The results for SF₆, which represent a range of free-stream pressures, show a forward displacement of the shock; the lower surface shock is absent. Clearly, this difference indicates a major weakness in the use of SF₆ to simulate compressible air flows. A scaling procedure to correct this problem has been developed in reference 5 for two-dimensional airfoils and is briefly reviewed next.

Transonic small-disturbance theory (ref. 11) yields a similarity parameter κ that takes the form

$$\kappa = \frac{1 - M_\infty^2}{[\tau M_\infty^2 (\gamma + 1)]^{2/3}} \quad (7)$$

If κ is computed for the desired Mach number in air, then the Mach number for SF₆ that yields the same value can be determined with a suitable definition of γ' . Reference 5 gives an appropriate definition,

$$\gamma' = 1 + \left(\frac{\partial a^2}{\partial h} \right)_{S, \infty} \quad (8)$$

This effective gamma varies with the free-stream temperature and pressure. Thus, the determination of an equivalent Mach number in SF₆ depends on these parameters as well as on the free-stream Mach number in air.

After the equivalent Mach number in SF₆ is determined and the results are obtained, the surface pressures, forces, and moments must be scaled to the original Mach number (that of air) by multiplying by the following factor (also obtained from transonic small-disturbance theory):

$$A = \frac{\gamma_{SF_6} + 1}{\gamma_{air} + 1} \frac{M_{SF_6}^2}{M_{air}^2} \frac{1 - M_{SF_6}^2}{1 - M_{air}^2} \quad (9)$$

The effectiveness of this Mach number scaling procedure on the previously described test case can be seen in figure 3. The lower surface shock is present, and the upper surface shock is in the correct location. The pressure distributions for SF₆ generally agree very well with the results for air. Note that the pressures agree well near the shocks, even though transonic small-disturbance theory (from which the scaling is derived) is generally valid only for isentropic, inviscid flows with small disturbances.

Test Cases

Two multielement airfoils are analyzed in the present work. Both were tested in air in the Langley Low-Turbulence Pressure Tunnel (LTPT) at Langley Research Center. (See ref. 12.) The first geometry (shown in fig. 4) is for a three-element airfoil that consists of a slat ahead of the main airfoil and a flap behind it. The slat and flap are both deflected downward by 30°. The thickness of the flap trailing edge on the wind-tunnel model is finite, but a wedge has been added to the trailing-edge geometry used for the computations to simplify the grid-generation process. The impact of this wedge on the results is minimized by making the trailing edge a point on the wake line as calculated by the panel method mentioned in the code description. The length of the wedge is approximately 1 percent of the total airfoil chord. The finest grid used for this geometry consists of 44837 nodes. The coordinates are given in tables I–III and are scaled with the chord length of the original airfoil with all high-lift elements stowed.

The second geometry, depicted in figure 5, is for a four-element configuration that is formed by deploying an auxiliary flap from the configuration described in the previous paragraph. The slat is in the same position as for the first geometry at a 30° deflection. The main flap is deflected by 36°, and the auxiliary flap is deflected by 50° (referenced to the main element). Again, a wedge has been added to the trailing edge of the auxiliary flap in the computations. The length of this wedge is also approximately 1 percent of the total airfoil chord. The finest grid for this geometry consists of 59788 nodes. The coordinates are given in tables I, II, IV, and V and reflect the

same coordinate scaling as for the three-element configuration.

Both geometries represent typical landing configurations with a low free-stream Mach number (0.2 in air) at a Reynolds number of 9×10^6 . The cases for SF₆ were run at a free-stream pressure of 10 atm and a free-stream temperature of 70°F. The scaled free-stream Mach number in SF₆ at these conditions is 0.222. Experimental data are available for angles of attack of 0° to the angle of maximum lift, which was approximately 23° for the three-element geometry and approximately 20° for the four-element geometry. The angles of attack used in this study correspond to data points in the wind-tunnel tests with corrections applied. (See ref. 12.) All computational results were run to a level of convergence sufficient to obtain steady distributions of surface pressure and skin-friction coefficients. In most cases, steady distributions were unattainable in the cove regions, and small fluctuations in the lift and drag coefficients are observed at high angles of attack (less than 1-percent maximum fluctuation). No experimental skin-friction and boundary-layer data are available for either geometry.

Results

Surface pressures for selected angles of attack are compared with experimental data in the section, "Surface Pressure." Skin-friction distributions and velocity profiles at a selected location are presented next, but these are comparisons of strictly computational results. For presentation of the surface-pressure and skin-friction distributions, the slat and flap elements are rotated to their undeflected positions, and the streamwise coordinate is normalized by the local chord of the airfoil element. The normal distance used for the velocity profiles is of the same scale as the grid (i.e., normalized by the chord of the airfoil with slat and flap(s) stowed). Finally, lift and drag coefficients are compared with experimental data.

Surface Pressure

Surface pressures are presented in figures 6–11 for each configuration at selected angles of attack. First, a baseline case at 0° is shown, followed by a midrange angle of attack and a case near the maximum-lift point (determined experimentally). The high-angle-of-attack cases exhibit small regions of supersonic flow and should represent a good test of both the computational method and the Mach number scaling procedure.

Figure 6 shows the distribution of surface-pressure coefficients for the three-element configuration at zero incidence. Excellent agreement with the experimental results is apparent except in the region of the slat cove. The computational results in this region are not expected

to agree well with experiment because the flow in this region is highly rotational and not properly modeled by the turbulence model. No significant differences are observed between the results for air and SF₆, regardless of whether the Mach number scaling is used.

Figure 7 shows surface-pressure distributions at an angle of attack of 8.109°. Again, the data agree well with the experiments; however, the experimental data in figure 7(c) indicate separation on the aft upper surface of the flap, whereas the calculations indicate attached flow. Still, little difference is seen between air and SF₆, regardless of scaling.

The high-angle-of-attack case (23.393°) is presented in figure 8. A small region of supersonic flow is evident on the slat upper surface, and the experimental data indicate that the flow over the flap is now attached. Minor differences in the suction peak are noted between the computations for air and SF₆ on the slat, where the case for air reaches a local Mach number value of 1.1. The Mach number scaling brings the results for SF₆ into closer agreement with those for air. No other significant differences are noted. The code predicts higher levels of suction pressure for the slat upper surface than those observed in the experiment; slightly lower levels are predicted for the flap upper surface. Agreement is excellent on the wing itself.

Figure 9 shows the baseline case of zero incidence for the four-element configuration. As with the three-element geometry, the computations agree well with the experimental data; almost no difference exists in the computational data except in the slat cove region, where the flow is highly rotational. Upper surface pressures on the slat are slightly underpredicted in comparison with the experimental data. The computational results for air and SF₆ are nearly identical.

The midrange angle of attack selected for the four-element configuration is 12.155°, and the results for this condition are shown in figure 10. Agreement with experiment for the slat is improved considerably, whereas the results on the main element slightly disagree with those from the experiments. Results for the flap agree well; however, the computational data show oscillations near the trailing edge of the auxiliary flap. As shown later in the skin-friction data, some separation at the trailing edge of the auxiliary flap may cause unsteadiness in the solution in this region.

The four-element configuration has a different maximum-lift angle of attack than the three-element configuration. This angle, as determined in the experiment, is 20.318°, and the results for this case are presented in figure 11. In a small region of supersonic flow on the slat upper surface, the local Mach number reaches a value of

1.21 for the case in which air is the test medium. A discrepancy is noted between the results for air and SF₆ in this region, and in contrast to the three-element geometry, the Mach number scaling does not significantly improve the results. Excellent agreement with experimental data is obtained for the slat and for the main element. Slightly higher levels of suction pressure are predicted for the upper surface of both flap elements, and the oscillations near the trailing edge of the auxiliary flap (fig. 11(d)) remain, again because of a small region of separation at the trailing edge of the auxiliary flap. As with the other cases, the three sets of computational data are virtually identical.

Skin Friction

To compute the skin-friction coefficient, the slope of the velocity profile must be calculated. This calculation is done by using a simple two-point divided difference with the boundary node on the surface and the next node off the surface. Because the grid has been generated initially from structured grids around each element, this node is approximately on a line normal to the surface at the boundary node. No scaling of the computed skin-friction coefficients in SF₆ is performed. Sample linear and logarithmic velocity profiles are shown in figure 12 for both the laminar inner and turbulent outer layers. The wake of the main element is visible and has begun to merge with the flap boundary layer. No significant differences are noted in the three curves.

Figure 13 shows the skin-friction coefficient distribution on the three-element configuration for the midrange angle of attack (8.109°). No significant differences are noted between the skin frictions computed in air and SF₆.

The high-angle-of-attack case (23.393°) is shown in figure 14. On the slat (fig. 14(a)), the unscaled results for SF₆ are significantly different from those of the other computations. This difference is attributed to a small region of supersonic flow on the slat. Greater discrepancies between the results for air and SF₆ are expected in such regions, regions where compressibility effects are important. The results for SF₆ at the scaled Mach number agree well with the results in air.

The skin-friction coefficient distribution for the midrange angle of attack for the four-element configuration (12.155°) is shown in figure 15. The same trends seen in the data for the three-element configuration are observed for this case. Two jumps in the skin-friction levels on the main flap (fig. 15(c)) are noted and are attributed to corresponding variations in the normal spacing of the first grid point off the surface. This spacing is generally very small (10^{-5} to 10^{-6}) and appears in the denominator of the skin-friction calculation. The skin-

friction calculation is therefore sensitive to chordwise variations of the grid spacing normal to the surface.

Figure 16 shows the results for the high-angle-of-attack case for the four-element configuration (20.318°). Similar to the high-angle-of-attack case for the three-element configuration, a difference between the unscaled results for SF₆ and the results for air is noted on the slat. (See fig. 16(a).) This difference is attributed to the small region of supersonic flow on this element. The Mach number scaling again brings the results back into agreement except for of a small region just aft of the suction peak. The two jumps in skin-friction levels on the main flap persist (fig. 16(c)), further indicating that the cause is associated with the grid.

Force Coefficients

The coefficients of lift and drag were computed by the flow solver as the sum of integrations of the surface-pressure and skin-friction coefficients over the surface of each element. Comparisons of computed lift and drag coefficients for the three-element configuration are shown versus angle of attack in figure 17. The computed lift coefficients agree well with the experimental data at lower angles of attack, but the code does not capture the stall point. The experimental data show a stall that is sharper and at a lower angle of attack than that in the computed data. The computed drag coefficients do not agree well with the experimental data, in spite of excellent agreement in the surface pressures. The use of SF₆ appears to have a greater effect on drag than on lift.

Figure 18 shows lift and drag coefficients for the four-element configuration. The general trends noted for this configuration are the same as those for the three-element configuration: the code does not capture the stall, the drag coefficients do not agree well with the experimental data, and the SF₆ affects drag more than it affects lift. Note, however, that for both geometries the use of the Mach number scaling brings the results for air and SF₆ into closer agreement.

Conclusions

A method for calculating viscous flows of sulfur hexafluoride (SF₆) over two-dimensional configurations has been developed and applied to two multielement airfoils. From the results presented here, several conclusions can be drawn about the suitability of SF₆ as a test medium for low Mach number flows over high-lift systems. First, the surface pressure coefficients computed in both air and SF₆ do not differ significantly except at small regions of supersonic flow on the leading element at high angles of attack. The inviscid Mach number scaling procedure adequately corrects for this discrepancy, which improves the agreement between the pressure and

skin-friction data for these cases. The boundary-layer data are also encouraging. No significant differences in the velocity profiles were noted.

The method used in this study cannot be used reliably to assess the effects of the use of SF₆ on such flow features as transition locations and possible flow separation. Nevertheless, the study provides results that are sufficiently encouraging to warrant further study in an experimental setting.

NASA Langley Research Center
Hampton, VA 23681-0001
February 21, 1995

References

1. Lynch, F. T.: Experimental Necessities for Subsonic Transport Configuration Development. AIAA-92-0158, Jan. 1992.
2. Meredith, P. T.: Viscous Phenomena Affecting High-Lift Systems and Suggestions for Future CFD Development. *High-Lift System Aerodynamics*, AGARD-CP-515, Oct. 1993.
3. Anders, John B.: *Heavy Gas Wind-Tunnel Research at Langley Research Center*. 93-FE-5, ASME, June 1993.
4. SF₆. SFBR-1, Allied Chemical Corp., 1976. (Replaces SFBR-1 dated 1973.)
5. Anderson, W. Kyle: *Numerical Study of the Aerodynamic Effects of Using Sulfur Hexafluoride as a Test Gas in Wind Tunnels*. NASA TP-3086, 1991.
6. Drela, Mark: *Modeling of Heavy-Gas Effects on Airfoil Flows*. NASA CR-190357, 1992.
7. Mavriplis, Dimitri J.: *Turbulent Flow Calculations Using Unstructured and Adaptive Meshes*. NASA CR-182012, ICASE Rep. No. 90-61, 1990. (Available from DTIC as AD-A227 793.)
8. Baldwin, Barrett; and Lomax, Harvard: Thin-Layer Approximation and Algebraic Model for Separated Turbulent Flows. AIAA-78-257, Jan. 1978.
9. Modell, Michael; and Reid, Robert C.: *Thermodynamics and Its Applications*, Second ed. Prentice-Hall, Inc., 1974.
10. Cook, P. H.; McDonald, M. A.; and Firmin, M. C. P.: Aerofoil RAE 2822—Pressure Distributions, and Boundary Layer and Wake Measurements. *Experimental Data Base for Computer Program Assessment*, AGARD-AR-138, May 1979, pp. A6-1–A6-77.
11. Liepmann, H. W.; and Roshko, A.: *Elements of Gasdynamics*. John Wiley & Sons, Inc., 1957.
12. Valarezo, Walter O.; Dominik, Chet J.; McGhee, Robert J.; Goodman, Wesley L.; and Paschal, Keith B.: Multi-Element Airfoil Optimization for Maximum Lift at High Reynolds Numbers. *Technical Papers—9th AIAA Applied Aerodynamics Conference*, Volume 2, 1991, pp. 969–976. (Available as AIAA-91-3332.)

Table I. Slat Coordinates Normalized by Chord Length

[Three- and four-element configurations]

X/c	Y/c	X/c	Y/c
0.144797	0.0464118	0.0412636	-0.0628568
.137522	.0394186	.0408055	-.0600636
.122576	.0253050	.0407555	-.0584764
.105312	.00520818	.0408250	-.0570973
.0931273	-.0136873	.0411045	-.0550818
.0856264	-.0306955	.0419036	-.0519655
.0825150	-.0473068	.0435423	-.0478036
.0857105	-.0607050	.0463064	-.0425909
.0894555	-.0644836	.0500182	-.0370205
.0943536	-.0665873	.0553455	-.0302468
.0997895	-.0667332	.0620259	-.0228186
.0957441	-.0682200	.0704255	-.0143668
.0882764	-.0702855	.0805705	-.00493864
.0806614	-.0720955	.0920832	.00512136
.0728182	-.0735109	.103778	.0148650
.0646159	-.0743041	.115612	.0243677
.0587927	-.0742182	.126760	.0330577
.0537614	-.0735032	.134775	.0391759
.0486732	-.0716905	.140813	.0437191
.0447614	-.0689155	.144797	.0464118
.0426050	-.0661805		

Table II. Wing Coordinates Normalized by Chord Length

[Three- and four-element configurations]

X/c	Y/c	X/c	Y/c
1.00012	0.0722791	0.196023	0.0591382
.976022	.0731241	.203522	.0635132
.951022	.0733441	.211523	.0675705
.926022	.0733441	.221023	.0717755
.901022	.0733441	.233523	.0765332
.876022	.0733441	.248523	.0813405
.826022	.0733441	.258523	.0840973
.826022	.0487264	.268523	.0865441
.826022	.0241086	.278522	.0885741
.806022	.0203905	.291022	.0901814
.776022	.0148518	.306022	.0916641
.726022	.00618091	.326022	.0934555
.651022	-.00419955	.351022	.0954241
.576022	-.0105845	.376022	.0971282
.501022	-.0131077	.426022	.0998405
.426022	-.0124736	.476022	.101734
.351022	-.00917955	.526022	.102870
.281022	-.00359227	.576022	.103263
.216023	.00446364	.626022	.102913
.196023	.00779364	.676022	.101816
.184022	.0101036	.726022	.0999564
.175023	.0139359	.776022	.0972891
.170835	.0199932	.826022	.0937364
.169835	.0246309	.851022	.0915923
.170835	.0318664	.876022	.0891832
.172523	.0361155	.901022	.0864891
.175023	.0403773	.926022	.0834905
.179022	.0454114	.951022	.0801582
.184022	.0503023	.976022	.0764682
.190023	.0550841	1.00012	.0722791

Table III. Flap Coordinates Normalized by Chord Length

[Three-element configuration]

X/c	Y/c	X/c	Y/c
1.25289	−0.0968750	0.993467	0.0529141
1.24986	−.0942468	.999262	.0577109
1.24076	−.0864691	1.00634	.0603014
1.22536	−.0743341	1.02141	.0608945
1.20344	−.0588286	1.03629	.0582118
1.19001	−.0501132	1.05077	.0538191
1.17492	−.0409377	1.06489	.0483736
1.15817	−.0314450	1.08552	.0389055
1.13977	−.0217673	1.10562	.0283623
1.11976	−.0120005	1.12530	.0170482
1.09818	−.00225227	1.14463	.00514136
1.07512	.00743909	1.16050	−.00515045
1.05069	.0170850	1.17661	−.0175995
1.03034	.0247368	1.19207	−.0308536
1.01195	.0314495	1.20557	−.0427977
.994987	.0375245	1.22262	−.0583368
.991311	.0405236	1.23613	−.0712227
.990120	.0451436	1.25582	−.0918159
.990473	.0475300	1.25289	−.0968750
.991371	.0497700	1.25289	−.0968750

Table IV. Main-Flap Coordinates Normalized by Chord Length

[Four-element configuration]

X/c	Y/c	X/c	Y/c
1.20101	−0.0505141	1.03039	0.0532795
1.18938	−.0422005	1.03925	.0528595
1.17095	−.0292945	1.04733	.0513159
1.16048	−.0219655	1.05371	.0495295
1.14974	−.0373041	1.05986	.0474245
1.14103	−.0327986	1.06585	.0450795
1.11925	−.0203168	1.07170	.0425400
1.09705	−.00843227	1.07858	.0392850
1.07451	.00296091	1.08599	.0354864
1.05170	.0139773	1.09414	.0310055
1.02871	.0247295	1.10280	.0259386
1.01435	.0313336	1.11554	.0179805
1.01107	.0344050	1.13624	.00395864
1.01015	.0391886	1.15643	−.0108027
1.01181	.0438477	1.17227	−.0230405
1.01605	.0484827	1.18463	−.0337295
1.01935	.0505882	1.19455	−.0435255
1.02353	.0522050	1.20101	−.0505141

Table V. Auxiliary-Flap Coordinates Normalized by Chord Length

[Four-element configuration]

X/c	Y/c	X/c	Y/c
1.26695	-0.174200	1.19029	-0.0566368
1.26256	-.166311	1.19477	-.0565295
1.25454	-.152660	1.19907	-.0578082
1.24878	-.143600	1.20461	-.0608591
1.24178	-.133186	1.21194	-.0667700
1.23348	-.121533	1.21820	-.0732332
1.22384	-.108749	1.22393	-.0801814
1.21280	-.0949659	1.22921	-.0874695
1.20031	-.0803168	1.23470	-.0960318
1.19767	-.0773105	1.23972	-.104877
1.19087	-.0697936	1.24502	-.114826
1.18724	-.0658755	1.25068	-.125716
1.18550	-.0636741	1.25645	-.137164
1.18481	-.0618705	1.26123	-.147047
1.18540	-.0597405	1.26499	-.155326
1.18635	-.0587086	1.26695	-.174200

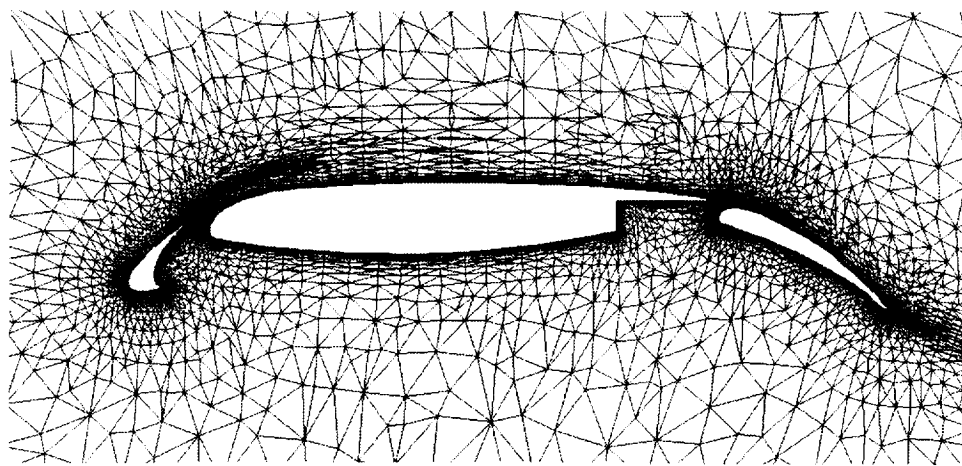


Figure 1. Portion of triangular mesh about three-element airfoil.

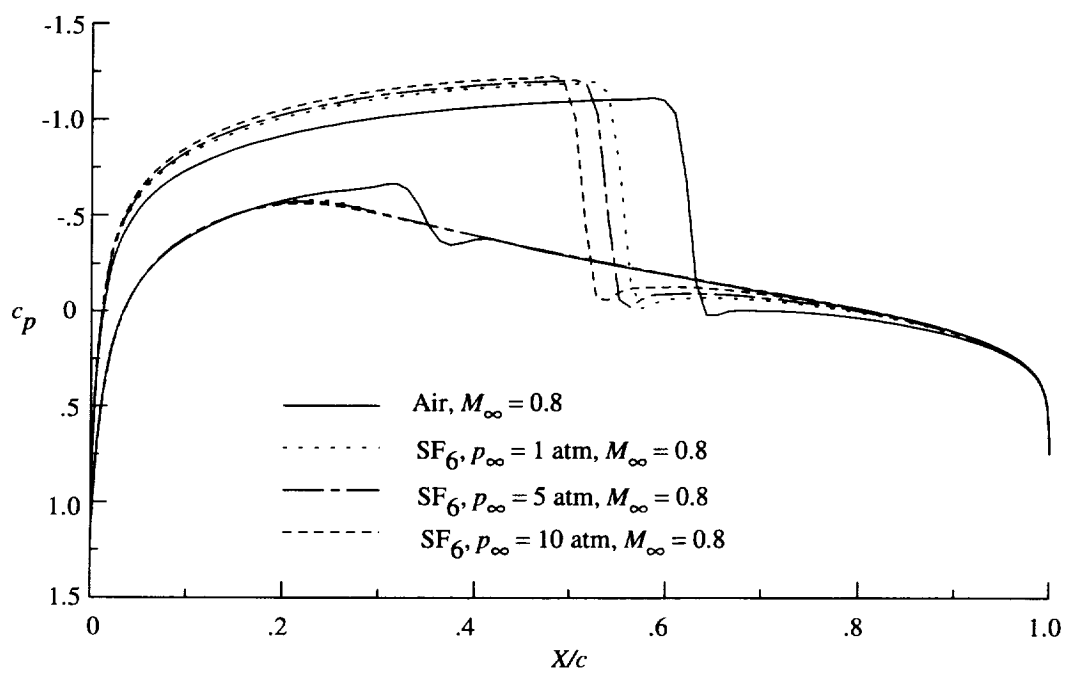


Figure 2. AGARD case 01 without Mach number scaling.

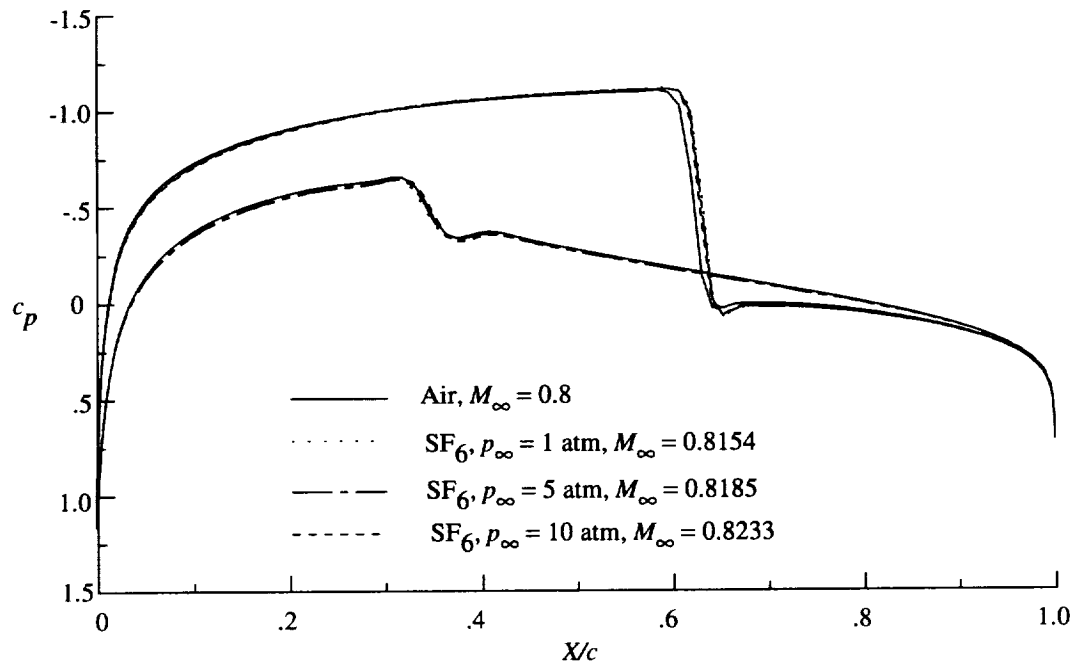


Figure 3. AGARD case 01 with Mach number scaling.

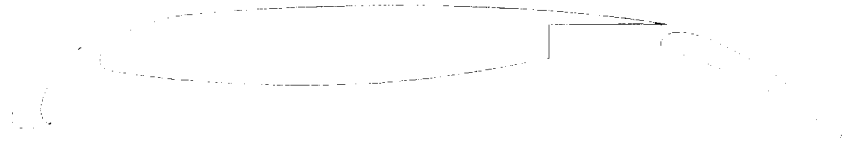


Figure 4. Three-element airfoil configuration.

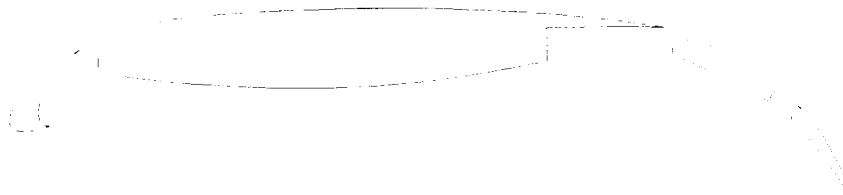
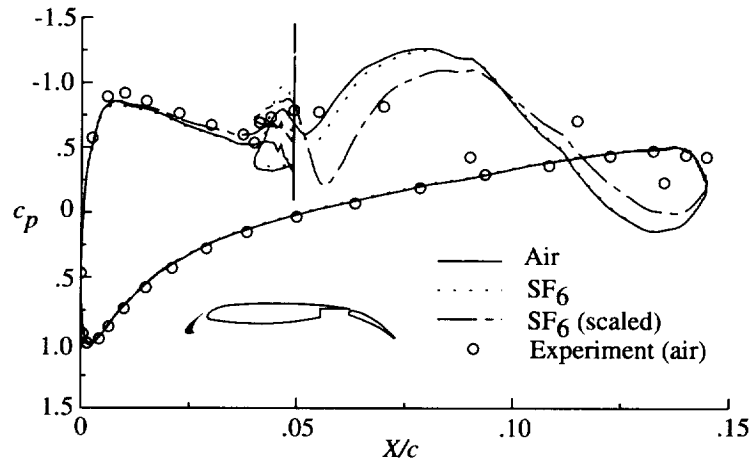
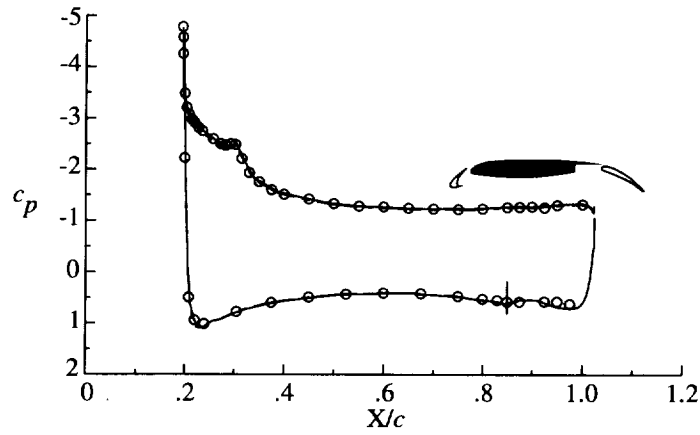


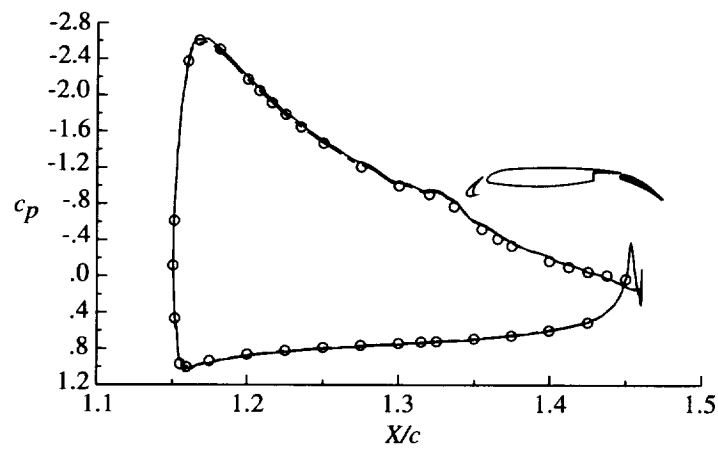
Figure 5. Four-element airfoil configuration.



(a) Slat.

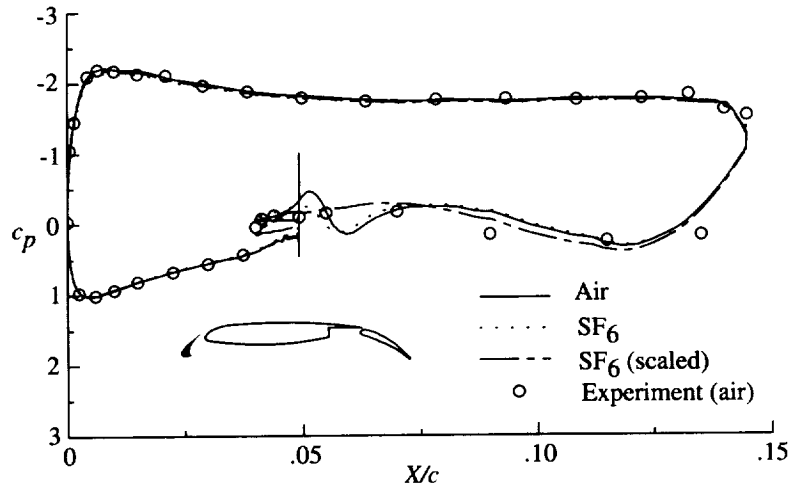


(b) Wing.

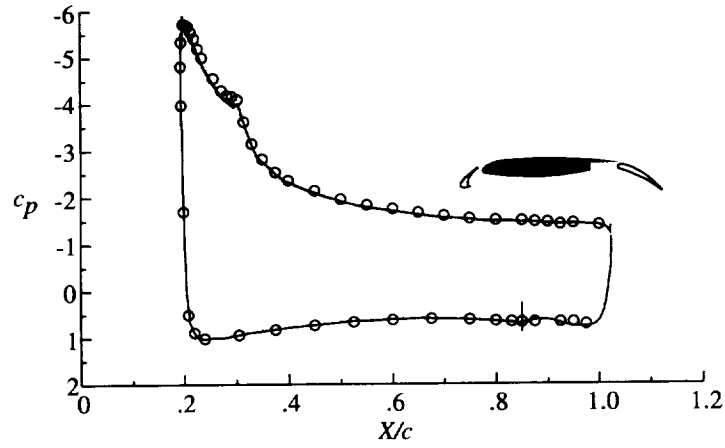


(c) Flap.

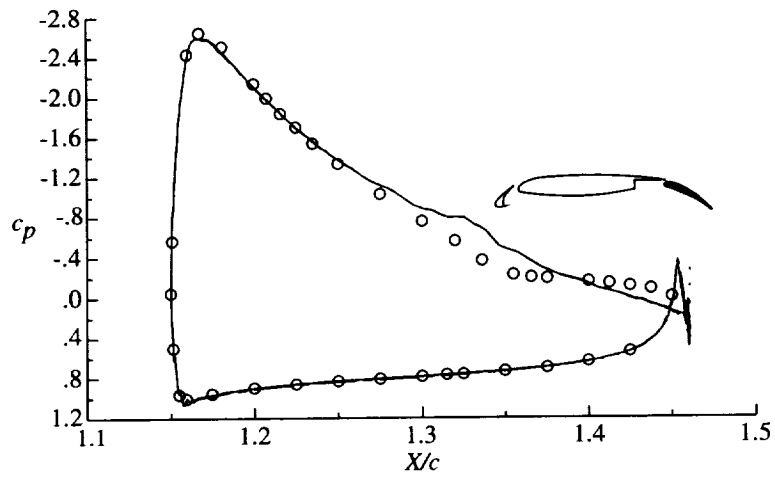
Figure 6. Distribution of surface-pressure coefficient on three-element airfoil with $\alpha = 0^\circ$, $M_\infty = 0.2$, and $N_{Re} = 9 \times 10^6$.



(a) Slat.

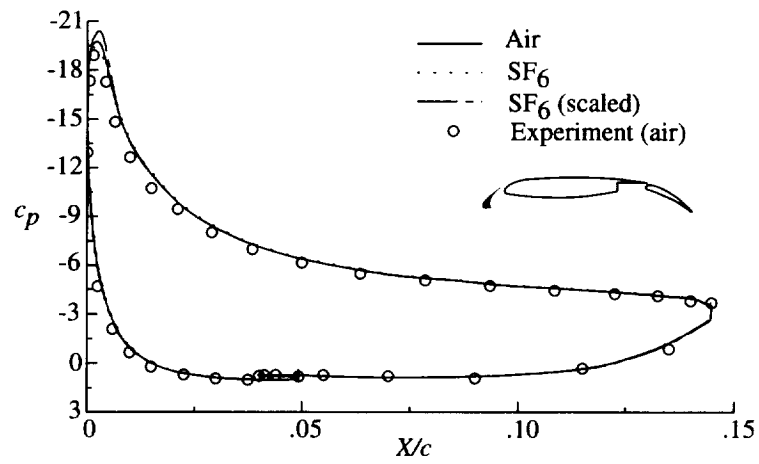


(b) Wing.

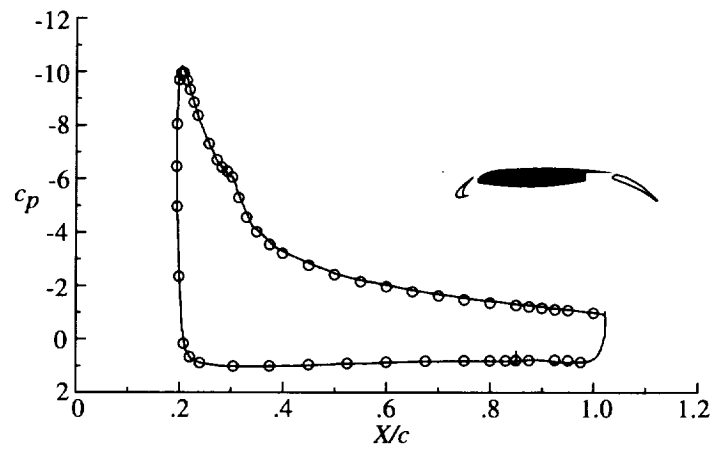


(c) Flap.

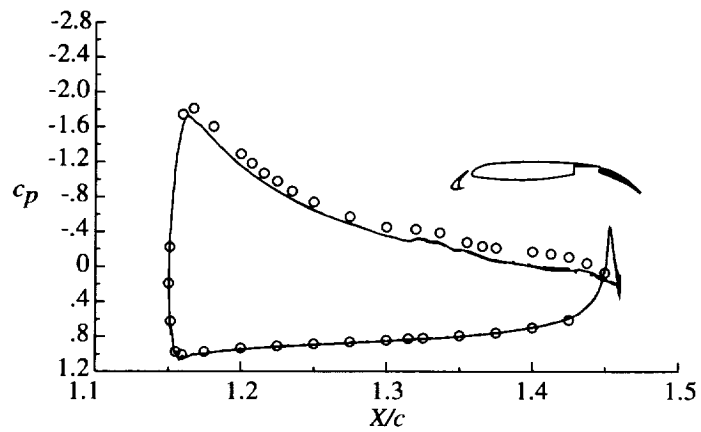
Figure 7. Distribution of surface-pressure coefficient on three-element airfoil with $\alpha = 8.109^\circ$, $M_\infty = 0.2$, and $N_{Re} = 9 \times 10^6$.



(a) Slat.

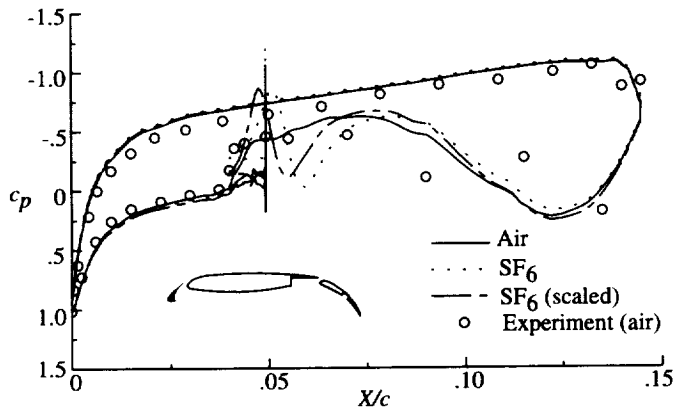


(b) Wing.

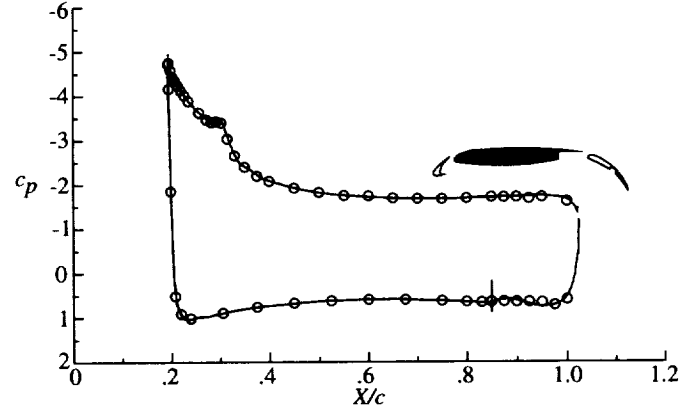


(c) Flap.

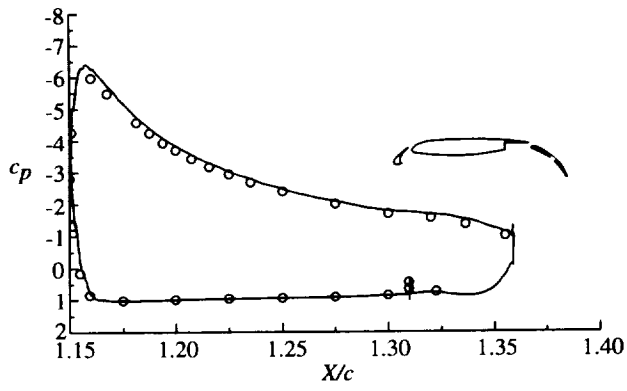
Figure 8. Distribution of surface-pressure coefficient on three-element airfoil with $\alpha = 23.393^\circ$, $M_\infty = 0.2$, and $N_{Re} = 9 \times 10^6$.



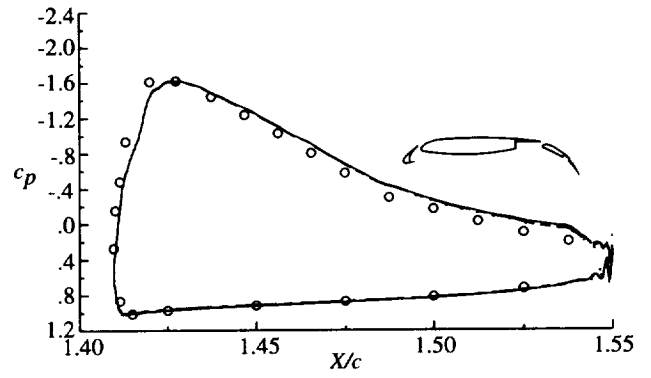
(a) Slat.



(b) Wing.



(c) Main flap.



(d) Auxiliary flap.

Figure 9. Distribution of surface-pressure coefficient on four-element airfoil with $\alpha = 0^\circ$, $M_\infty = 0.2$, and $N_{Re} = 9 \times 10^6$.

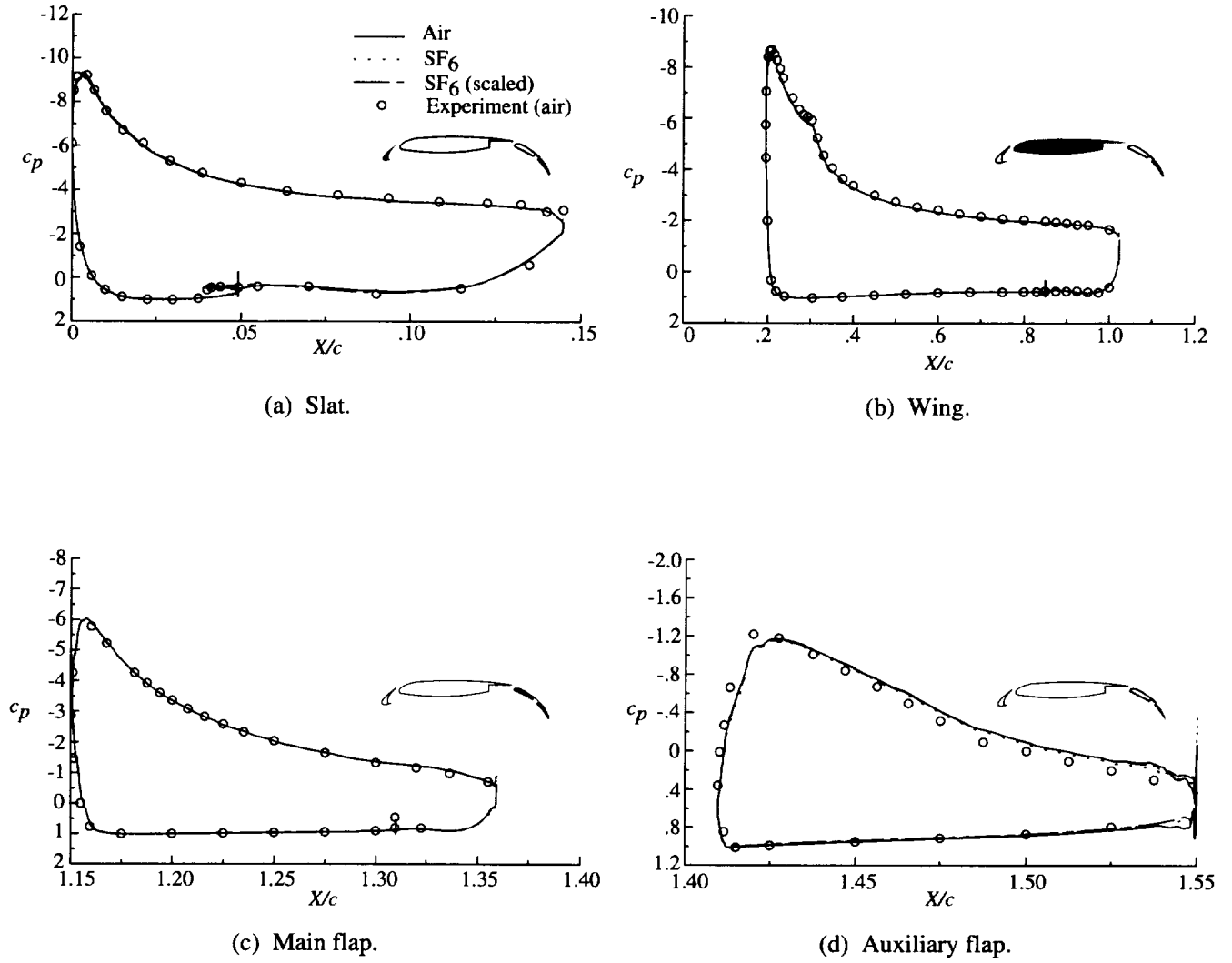
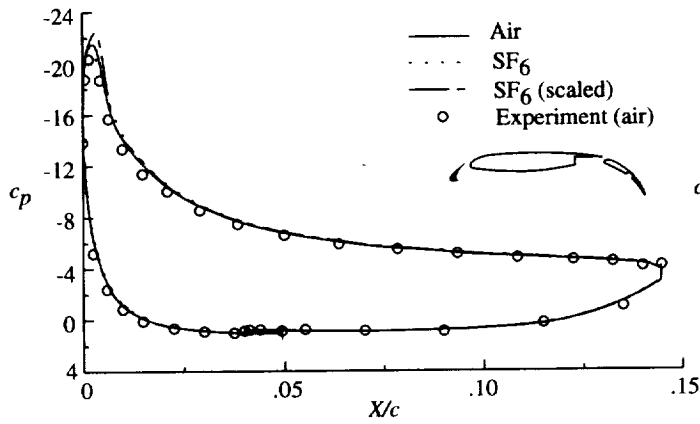
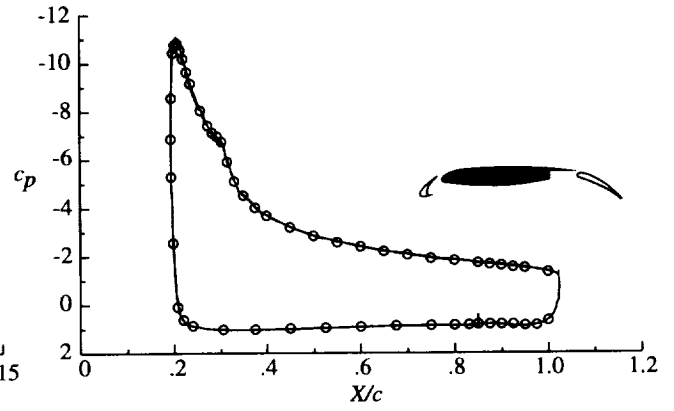


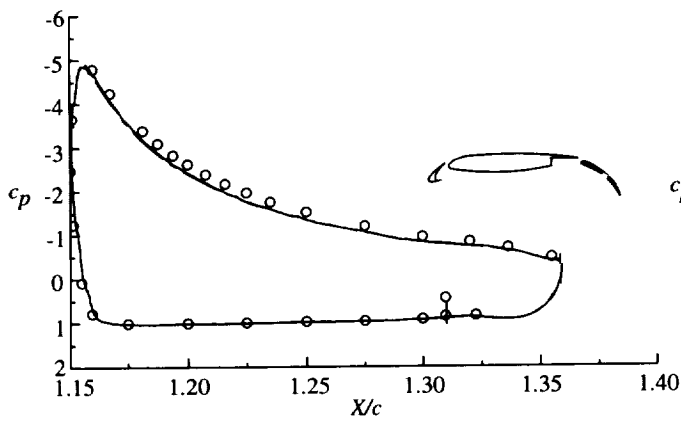
Figure 10. Distribution of surface-pressure coefficient on four-element airfoil with $\alpha = 12.155^\circ$, $M_\infty = 0.2$, and $N_{Re} = 9 \times 10^6$.



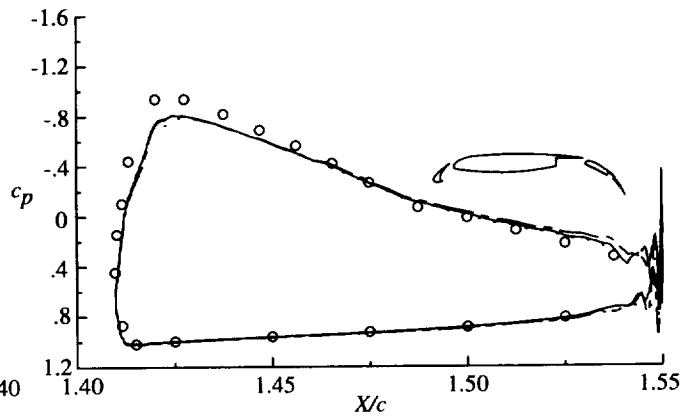
(a) Slat.



(b) Wing.

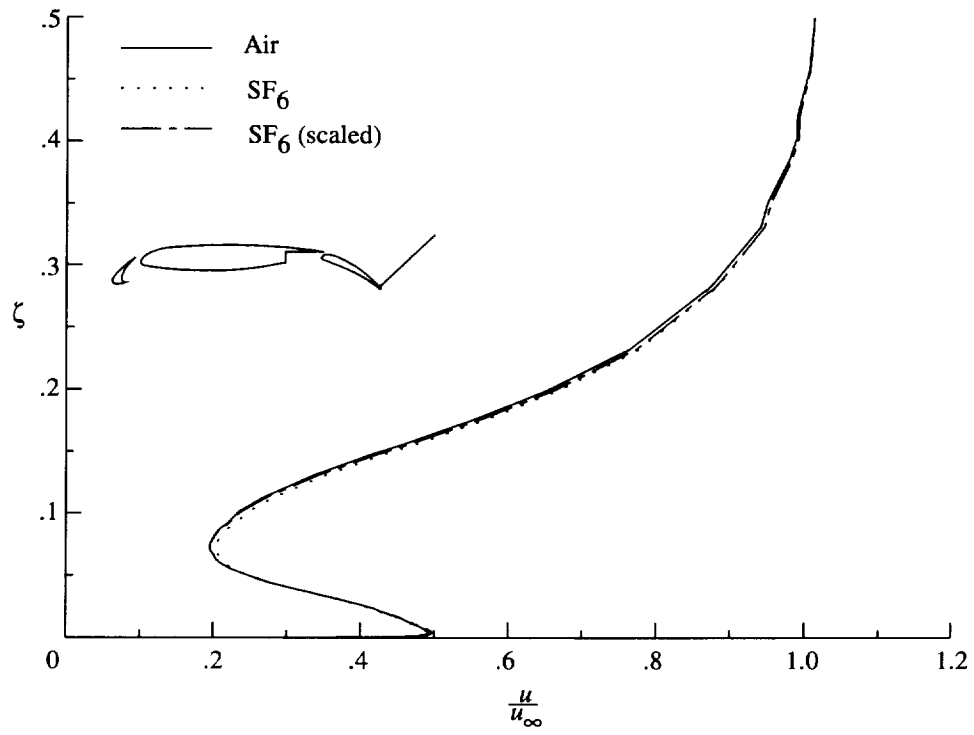


(c) Main flap.

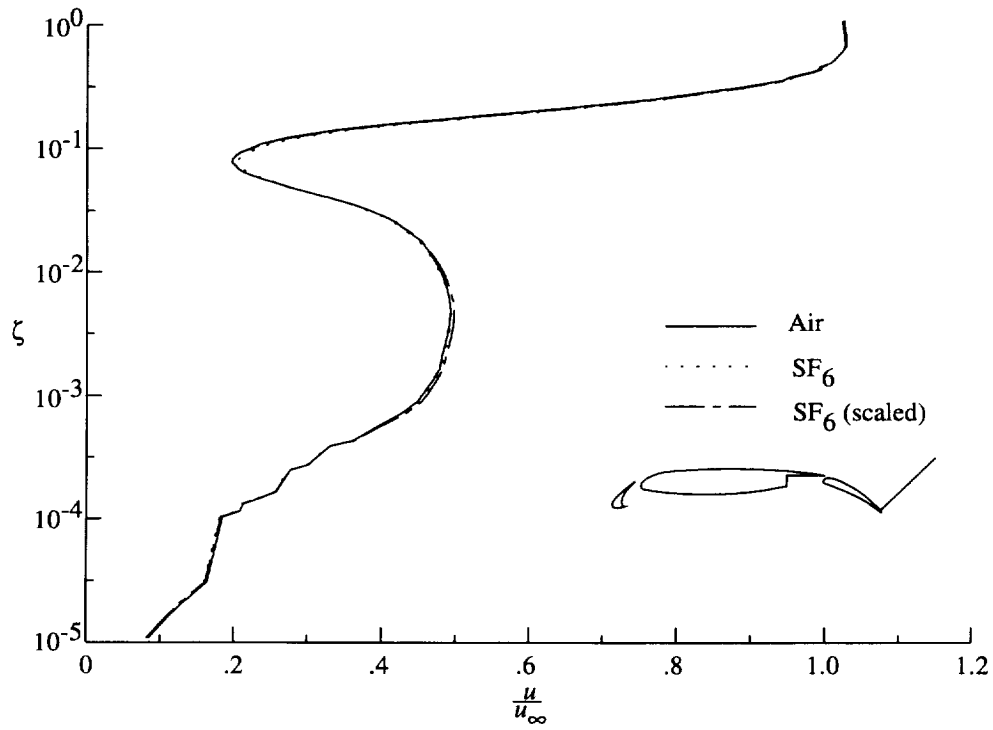


(d) Auxiliary flap.

Figure 11. Distribution of surface-pressure coefficient on four-element airfoil with $\alpha = 20.318^\circ$, $M_\infty = 0.2$, and $N_{Re} = 9 \times 10^6$.

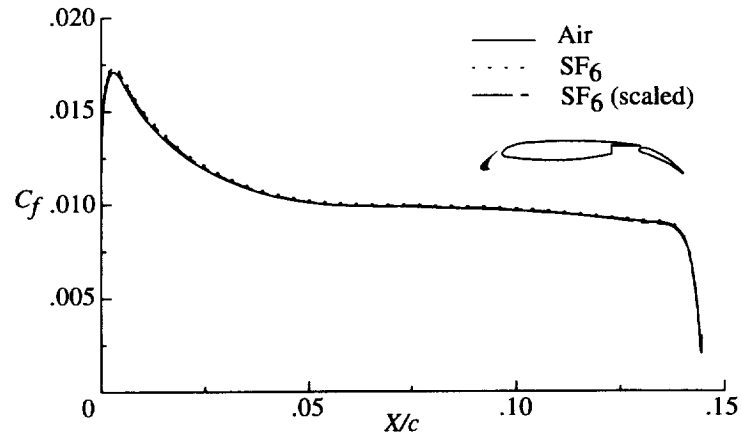


(a) Linear scale.

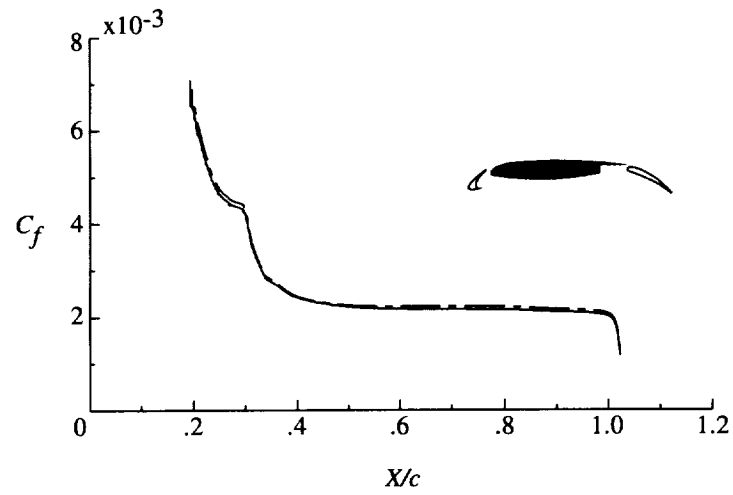


(b) Logarithmic scale.

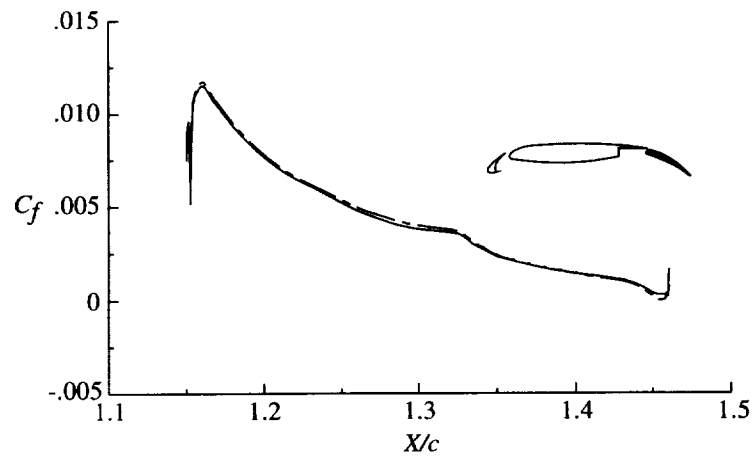
Figure 12. Velocity profile for three-element configuration at $x = 1.25$.



(a) Slat.

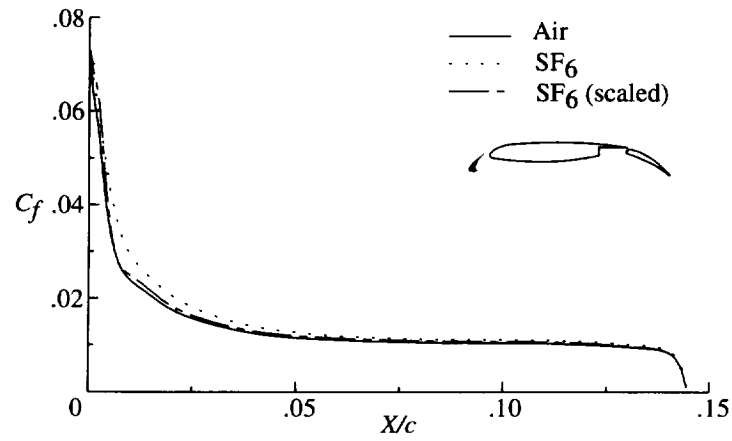


(b) Wing.

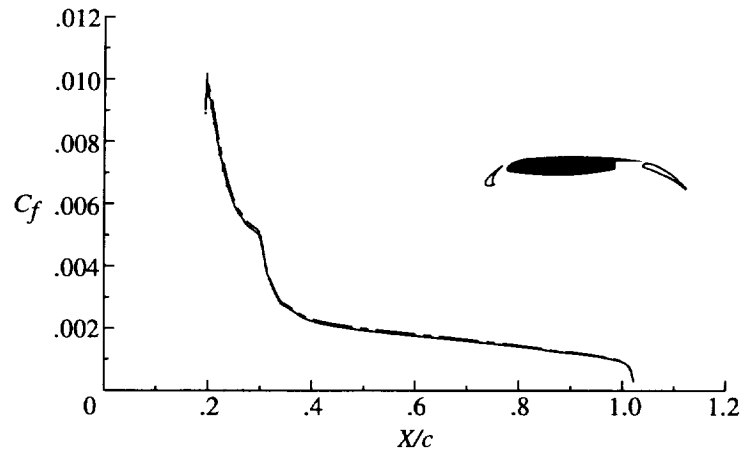


(c) Flap.

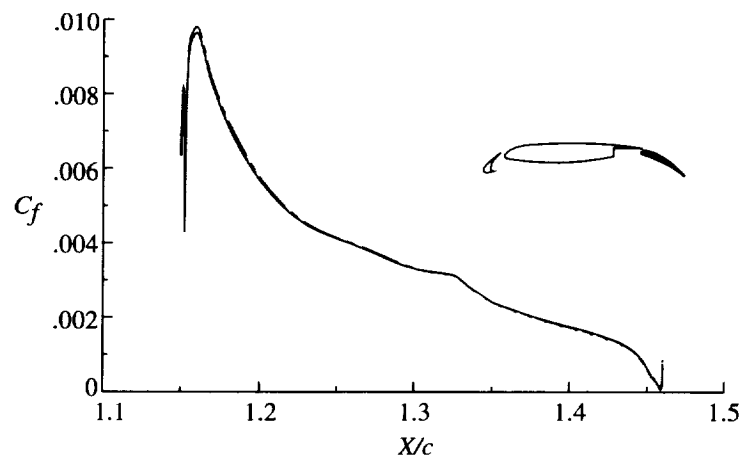
Figure 13. Distribution of skin-friction coefficient on three-element airfoil with $\alpha = 8.109^\circ$, $M_\infty = 0.2$, and $N_{Re} = 9 \times 10^6$.



(a) Slat.



(b) Wing.



(c) Flap.

Figure 14. Distribution of skin-friction coefficient on three-element airfoil with $\alpha = 23.393^\circ$, $M_\infty = 0.2$, and $N_{Re} = 9 \times 10^6$.

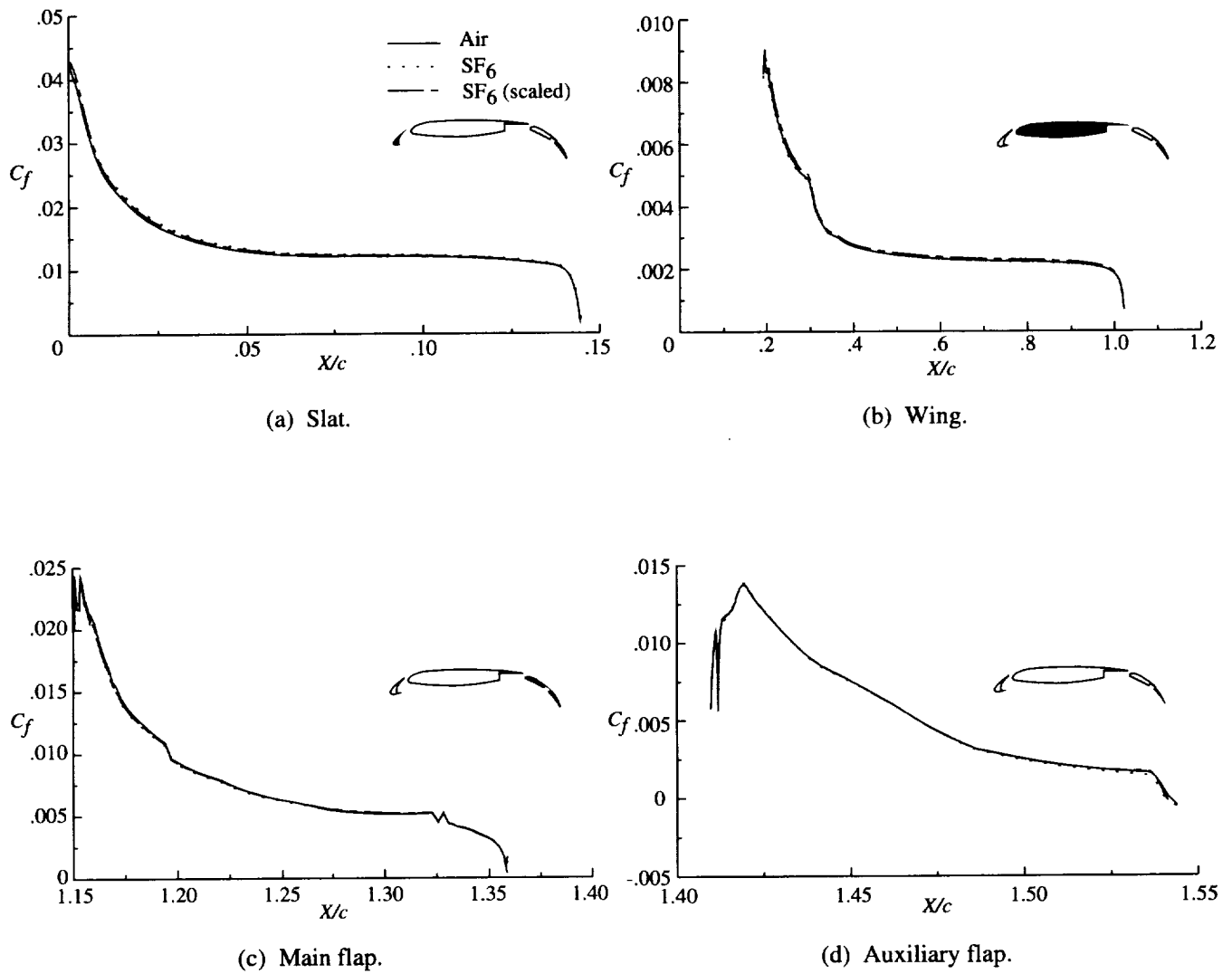


Figure 15. Distribution of skin-friction coefficient on four-element airfoil with $\alpha = 12.155^\circ$, $M_\infty = 0.2$, and $N_{Re} = 9 \times 10^6$.

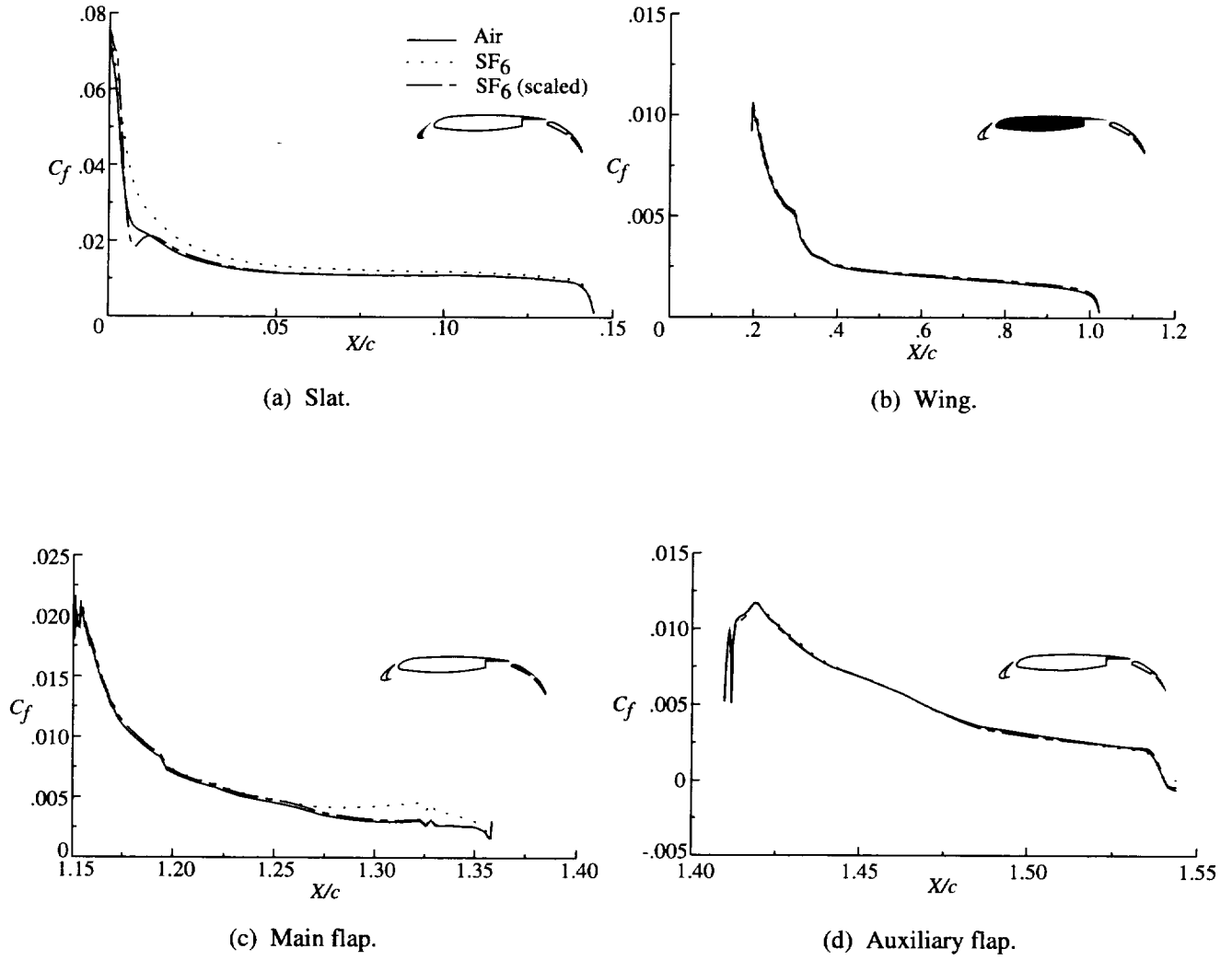
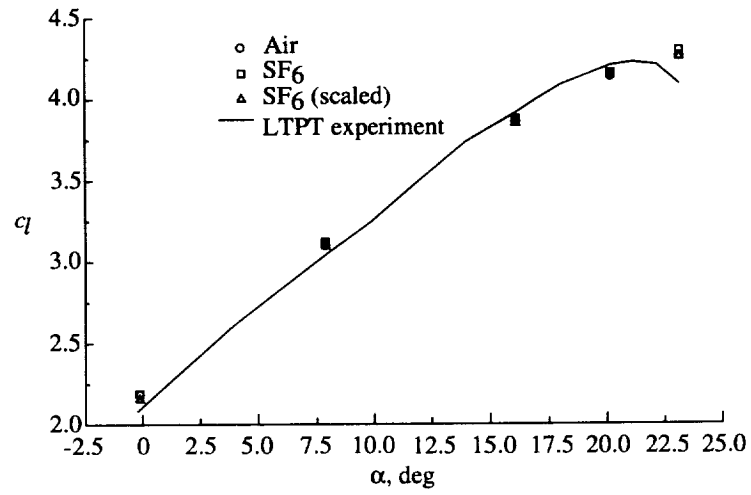
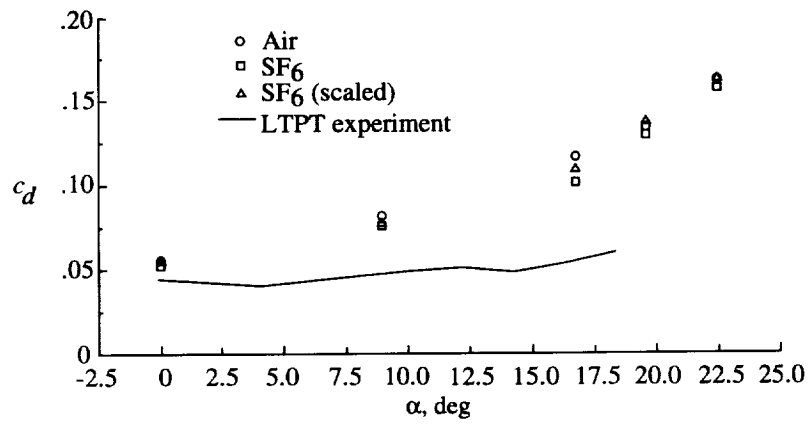


Figure 16. Distribution of skin-friction coefficient on four-element airfoil with $\alpha = 20.318^\circ$, $M_\infty = 0.2$, and $N_{Re} = 9 \times 10^6$.

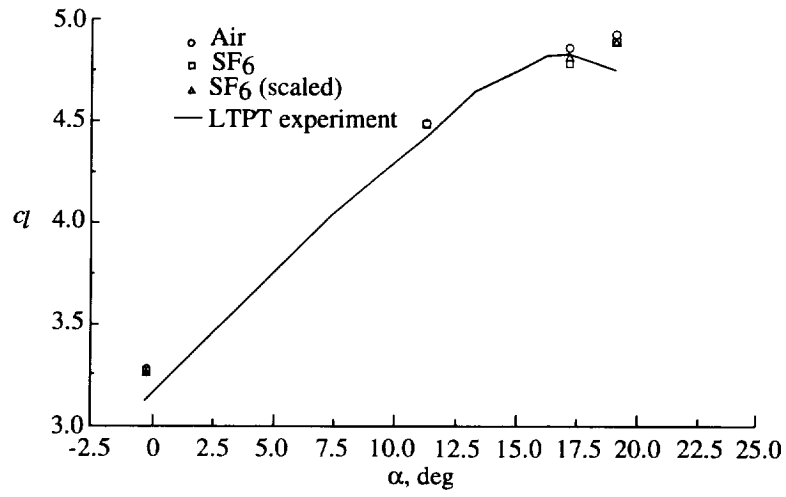


(a) Lift.

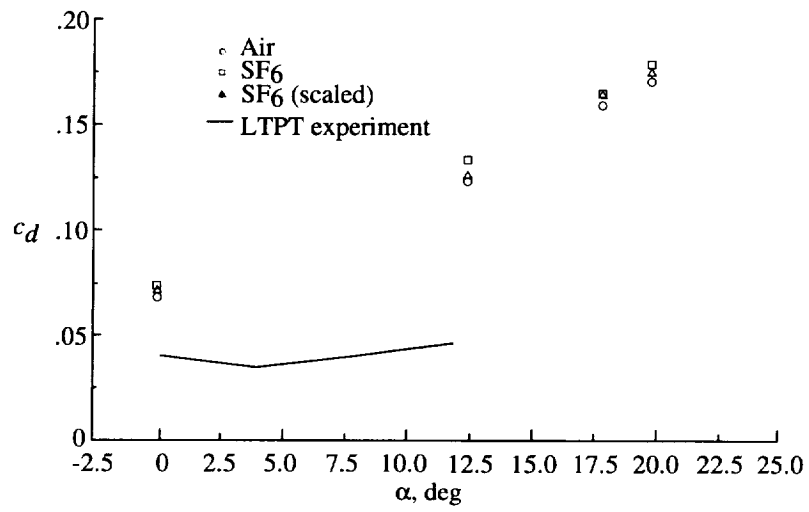


(b) Drag.

Figure 17. Force coefficients for three-element configuration versus angle of attack.



(a) Lift.



(b) Drag.

Figure 18. Force coefficients for four-element configuration versus angle of attack.

REPORT DOCUMENTATION PAGE			Form Approved OMB No. 0704-0188	
Public reporting burden for this collection of information is estimated to average 1 hour per response, including the time for reviewing instructions, searching existing data sources, gathering and maintaining the data needed, and completing and reviewing the collection of information. Send comments regarding this burden estimate or any other aspect of this collection of information, including suggestions for reducing this burden, to Washington Headquarters Services, Directorate for Information Operations and Reports, 1215 Jefferson Davis Highway, Suite 1204, Arlington, VA 22202-4302, and to the Office of Management and Budget, Paperwork Reduction Project (0704-0188), Washington, DC 20503.				
1. AGENCY USE ONLY (Leave blank)	2. REPORT DATE June 1995	3. REPORT TYPE AND DATES COVERED Technical Paper		
4. TITLE AND SUBTITLE Numerical Study To Assess Sulfur Hexafluoride as a Medium for Testing Multielement Airfoils		5. FUNDING NUMBERS WU 505-59-53-01		
6. AUTHOR(S) Daryl L. Bonhaus, W. Kyle Anderson, and Dimitri J. Mavriplis				
7. PERFORMING ORGANIZATION NAME(S) AND ADDRESS(ES) NASA Langley Research Center Hampton, VA 23681-0001		8. PERFORMING ORGANIZATION REPORT NUMBER L-17401		
9. SPONSORING/MONITORING AGENCY NAME(S) AND ADDRESS(ES) National Aeronautics and Space Administration Washington, DC 20546-0001		10. SPONSORING/MONITORING AGENCY REPORT NUMBER NASA TP-3496		
11. SUPPLEMENTARY NOTES Bonhaus and Anderson: Langley Research Center, Hampton, VA; Mavriplis: Institute of Computer Applications in Science and Engineering, Langley Research Center, Hampton, VA.				
12a. DISTRIBUTION/AVAILABILITY STATEMENT Unclassified-Unlimited Subject Category 02 Availability: NASA CASI (301) 621-0390		12b. DISTRIBUTION CODE		
13. ABSTRACT (Maximum 200 words) A methodology is described for computing viscous flows of air and sulfur hexafluoride (SF ₆). The basis is an existing flow solver that calculates turbulent flows in two dimensions on unstructured triangular meshes. The solver has been modified to incorporate the thermodynamic model for SF ₆ and used to calculate the viscous flow over two multielement airfoils that have been tested in a wind tunnel with air as the test medium. Flows of both air and SF ₆ at a free-stream Mach number of 0.2 and a Reynolds number of 9×10^6 are computed for a range of angles of attack corresponding to the wind-tunnel test. The computations are used to investigate the suitability of SF ₆ as a test medium in wind tunnels and are a follow-on to previous computations for single-element airfoils. Surface-pressure, lift, and drag coefficients are compared with experimental data. The effects of heavy gas on the details of the flow are investigated based on computed boundary-layer and skin-friction data. In general, the predictions in SF ₆ vary little from those in air. Within the limitations of the computational method, the results presented are sufficiently encouraging to warrant further experiments.				
14. SUBJECT TERMS Computational aerodynamics; Wind-tunnel testing; Heavy gas; Multielement airfoils			15. NUMBER OF PAGES 28	
			16. PRICE CODE A03	
17. SECURITY CLASSIFICATION OF REPORT Unclassified	18. SECURITY CLASSIFICATION OF THIS PAGE Unclassified	19. SECURITY CLASSIFICATION OF ABSTRACT Unclassified	20. LIMITATION OF ABSTRACT	